SUPPLEMENTARY

RHEOLOGY AND COAXIAL EXTRUSION OF ACELLULAR AND CELL-LADEN HOLLOW CONDUITS OF PRISTINE AND GOLD NANOCOMPOSITE KAPPA CARRAGEENAN HYDROGELS

Sanchari Swarupa [a], Mata Subhashita [b], Nikita Chauhan [c], Jitendra Bahadur [c, d], Sharad Gupta [a], Prachi Thareja [b, e*]

[a] Department of Biological Sciences and Engineering, IIT Gandhinagar, Palaj, Gujarat 382355, India

[b] Department of Chemical Engineering, IIT Gandhinagar, Palaj, Gujarat 382355, India

[c] Solid State Physics Division, Bhabha Atomic Research Centre, Mumbai, 400085, India

[d] Homi Bhabha National Institute, Anushaktinagar, Mumbai, 400094, India

[e] Dr. Kiran C. Patel Centre for Sustainable Development, IIT Gandhinagar, Palaj, Gujarat 382355, India

*Corresponding author: prachi@iitgn.ac.in

1. Hydrodynamic size measurement of $^{\kappa}$CG capped AuNPs in various compositions of $^{\kappa}$CG hydrogel

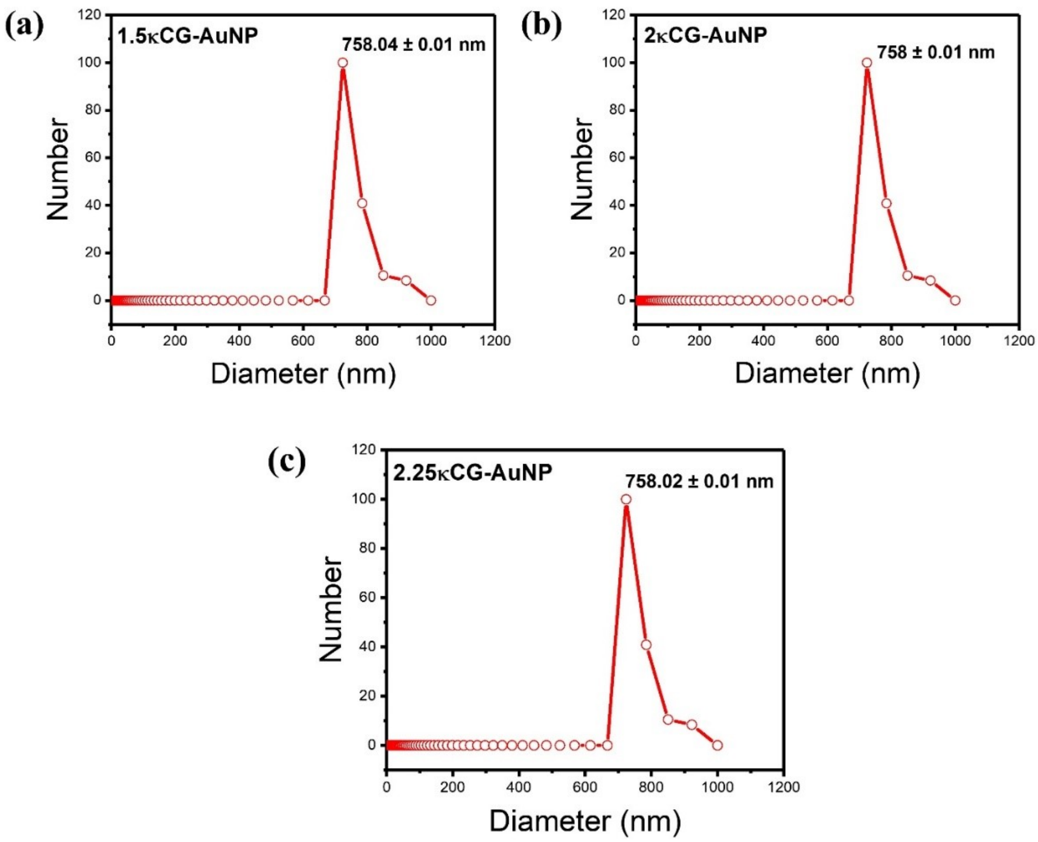

Fig S1. (a), (b) and (c) Number weighted (red empty circle) size distribution for *in situ* synthesized AuNPs in different compositions of pre-extruded κCG hydrogels.

2. Fourier Transform Infrared Spectroscopy (FTIR)

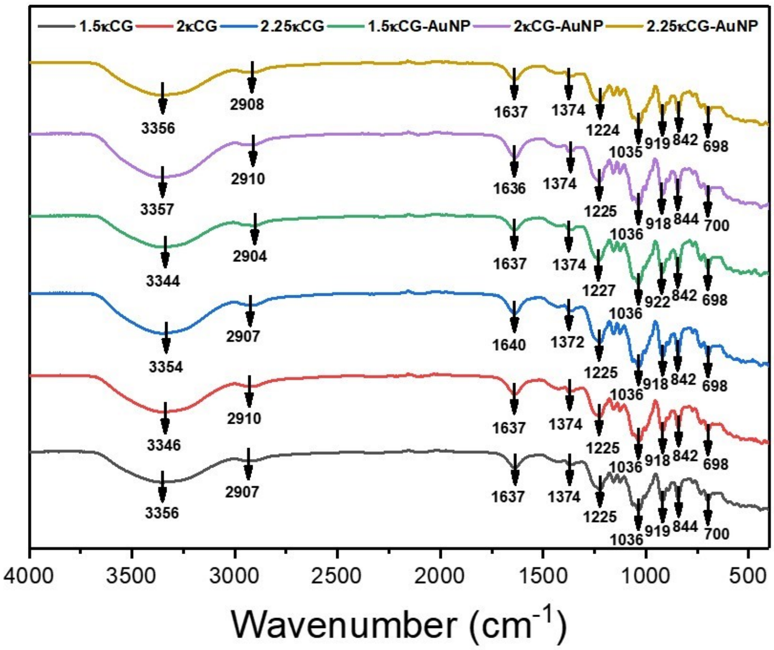

Fig S2. FTIR spectra of lyophilized κCG and κCG-AuNP hydrogels.

3. Small angle X-ray scattering (SAXS) studies

X-ray scattering studies of pristine κCG and κCG-AuNP hydrogels were carried out at the small/wide-angle X-ray scattering (SWAXS) beamline (BL-18) of Indus-2 synchrotron source located at RRCAT, Indore, India. A double-crystal Si (111) monochromator operated in non-dispersive mode was employed to tune X-ray energies between 5 and 20 keV, with an energy resolution of 10^{-3}. The monochromatic beam was then directed onto a 1.5 m toroidal mirror consisting of a silicon substrate coated with 60 nm Pt and 5 nm Rh, providing sagittal and meridional focusing. Scattering data were recorded using an online image-plate area detector over a Q-range of 0.06-3.5 nm-1 and a sample-to-detector distance of ~3 m. Radially averaged intensity profiles, I(Q), were obtained after instrument resolution correction, background subtraction and transmission normalization. The scattering angle is defined as 2θ, and the X-ray wavelength of 1.033 Å was employed, corresponding to 12 keV.

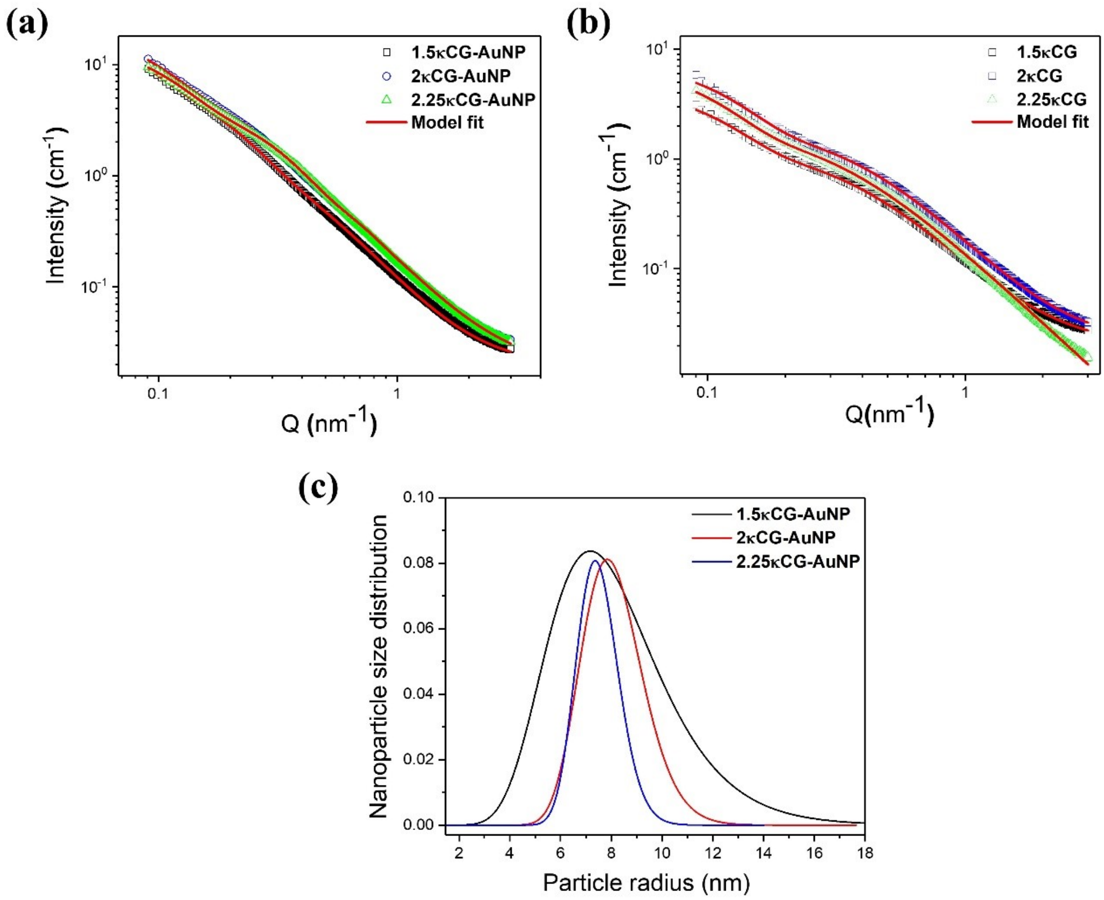

Fig S3. SAXS pattern of **(a)** κCG-AuNP hydrogels, **(b)** pristine κCG hydrogels (Hollow symbols represent the experimental data and solid lines show the model fit), **(c)** Nanoparticle size distribution of AuNP within different compositions of κCG.

Table S1. Fitting parameters of κCG-AuNP hydrogels.

Sample	**C1**	**$I_G(0)$**	**$I_L(0)$**	**R_g (nm)**	**ξ (nm)**	**D**	**C2**	**Avg. AuNP radius (nm)**
1.5κCG-AuNP	35.0	12.9	1.6	17.0	2.2	2.6	3.0	7.8
2κCG-AuNP	37.8	11.0	1.4	19.5	2.3	2.6	4.2	8.0
2.25κCG-AuNP	23.8	19.2	4.6	17.7	3.1	2.4	1.8	7.5

Table S2. Fitting parameters of pristine κCG hydrogels.

Sample	**$I_G(0)$**	**$I_L(0)$**	**R_g (nm)**	**ξ (nm)**	**D**
1.5κCG	12.3	4.6	16.7	2.5	2.5
2κCG	17.6	5.8	15.8	2.5	2.3
2.25κCG	15.5	5.4	17.8	3.1	2.2

Unlike a concentrated polymer solution, the internal structure of a polymer gel is characterized by multiple intrinsic length scales reflecting distinct modes of chain organization. At short length scales, the polymer network exhibits rapid, thermally driven concentration fluctuations, which are described by a correlation length ξ. These fluctuations arise from local segmental motion of polymer chains required to maintain thermodynamic equilibrium and are well captured by an Ornstein–Zernike (Lorentzian) formalism.

At larger length scales, the gel structure is governed by static heterogeneities originating from polymer segments that are immobilized or constrained by network junctions, crosslinks, or clusters of such junctions. These spatially frozen density inhomogeneities are characterized by a second length scale, denoted here as R_g, and are appropriately described using a Guinier-type model, analogous to scattering from finite-sized polymer-rich domains.

The relative weight of these two structural contributions is quantified by the zero-angle scattering intensities $I_L(0)$ and $I_G(0)$, parameterized as lorentz_scale and guinier_scale, respectively. The total scattered intensity is thus expressed as a superposition of dynamic and static contributions:

The scattered intensity I(q) is calculated as

$$I(Q) = \frac{I_L(0)}{\left(1 + [(D+1)/3]Q^2\xi^2\right)^{D/2}} + I_G(0)\exp\left(-\frac{Q^2 Rg^2}{3}\right) + B \qquad (1)$$

where Q is the scattering vector, D is the fractal dimension of the polymer network, and B accounts for the incoherent background. The first term reduces to the classical Ornstein–Zernike expression when the fractal dimension D=2, corresponding to a Flory exponent of 0.5 under theta-solvent conditions. Deviations from this ideal case reflect changes in chain statistics and interaction strength. In polymer gels where specific interactions such as hydrogen bonding play a significant role, the effective fractal dimension is often higher, with reported values in the range D≈2.6–2.8, indicative of more compact and strongly correlated network structures. This two-length-scale scattering framework provides a physically transparent means to disentangle dynamic concentration fluctuations from static network heterogeneities, offering deep insight into the hierarchical organization of polymer gels across nanometer to mesoscopic length scales.

For *in situ* synthesised AuNPs in hydrogels, the scattering contribution from AuNPs is added:

$$I(Q) = C_1\left[\frac{I_L(0)}{\left(1+[(D+1)/3]Q^2\xi^2\right)^{D/2}} + I_G(0)\exp\left(-\frac{Q^2Rg^2}{3}\right) + B\right] + C_2\int D(r)P(Q,r)r^3dr$$

(2)

Where P (Q, r) is the form factor for spherical AuNPs (eq. 2) with radius r whereas D(r) represents the AuNP size distribution. We have assumed a lognormal distribution for nanoparticle size.

$$P(Q,r) = 9\left[\frac{\sin(Qr) - QR\cos(Qr)}{(Qr)^3}\right]^2 \tag{2}$$

$$D(r) = \frac{1}{\sqrt{2\pi\sigma^2 r^2}}\exp\left[-\frac{\left(\ln(r/r_0)\right)^2}{2\sigma^2}\right] \tag{3}$$

Where r_0 is the median AuNP radius and σ is the polydispersity index of the size distribution. The average size can be expressed as $r_0 \exp(\sigma^2/2)$.

4. **Images of cross sections of coaxially extruded 1.5κCG-AuNP and 1.5κCG hydrogels**

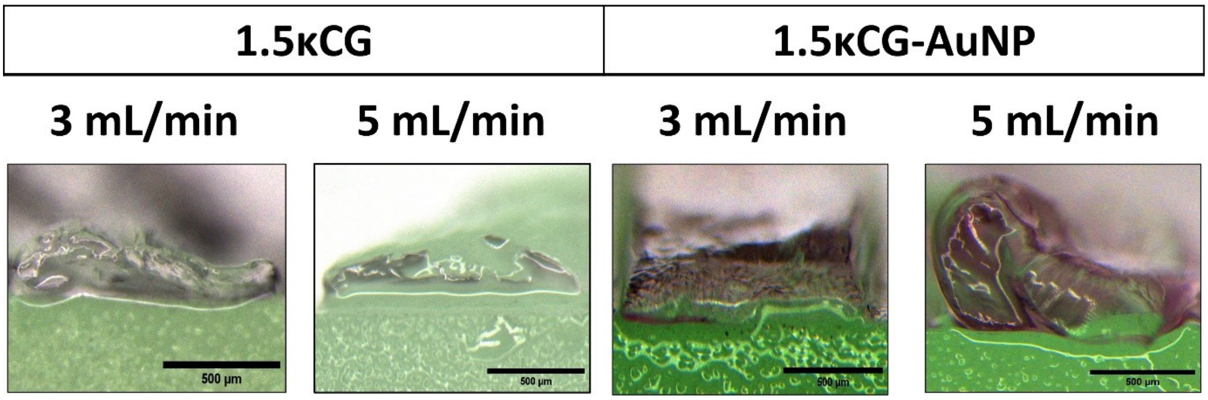

Fig S4. (a) and (b) Morphology of extruded filaments of κCG-AuNP and pristine κCG hydrogels after incubation in 100 mM KCl bath (Scale bar: 1 cm); **(c)** Stereomicroscopic images of cross-sections of coaxially extruded channels of 1.5κCG-AuNP and 1.5κCG hydrogels at two flow rates (Scale bar: 500 µm).

5. **Amplitude Sweep of pre-extruded and post-extruded hydrogels at 37 °C and 25 °C**

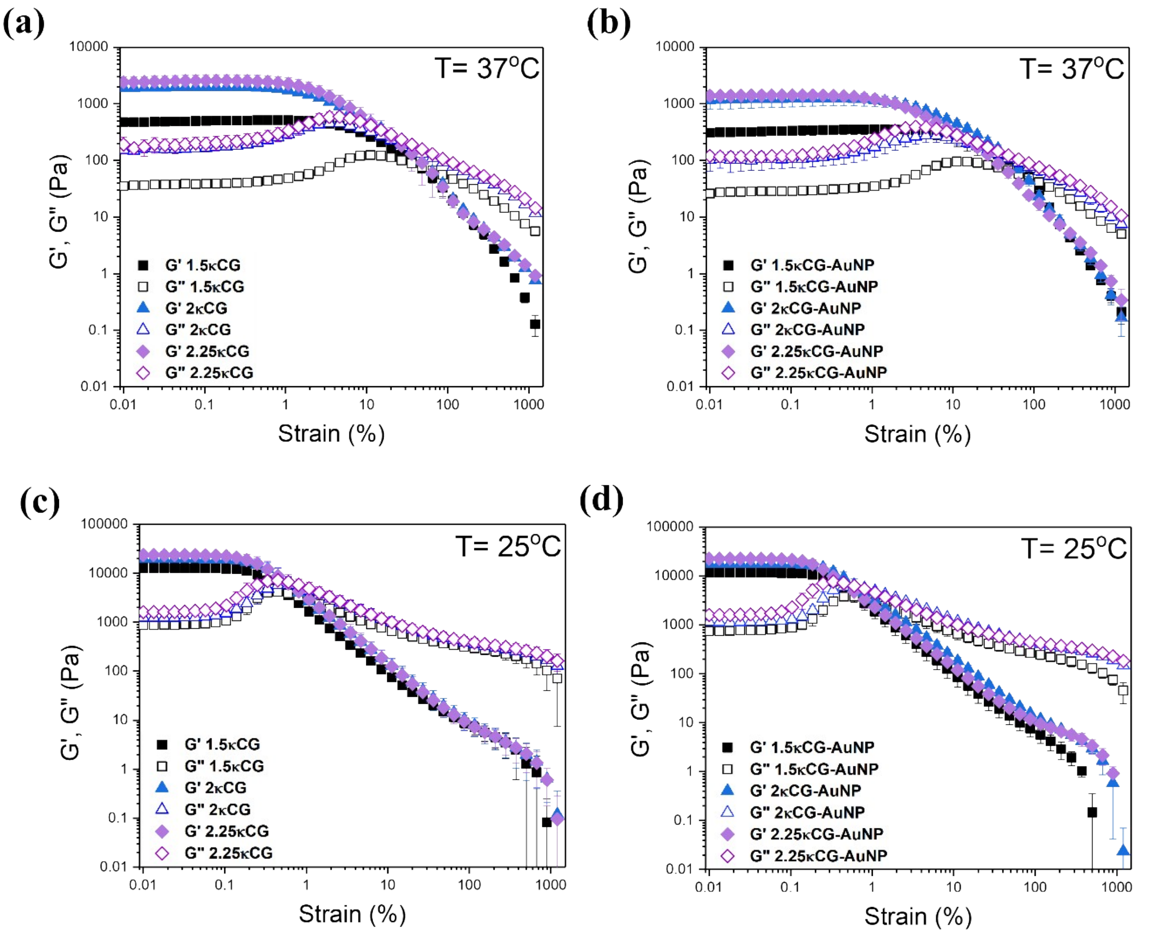

Fig S5. Large amplitude oscillatory strain sweeps of all compositions of **(a)** pristine κCG and **(b)** κCG-AuNP, and crosslinked in 100 mM KCl bath **(c)** pristine κCG and **(d)** κCG-AuNP hydrogels.

6. **Power law fits of pre-extruded hydrogels at 37 °C**

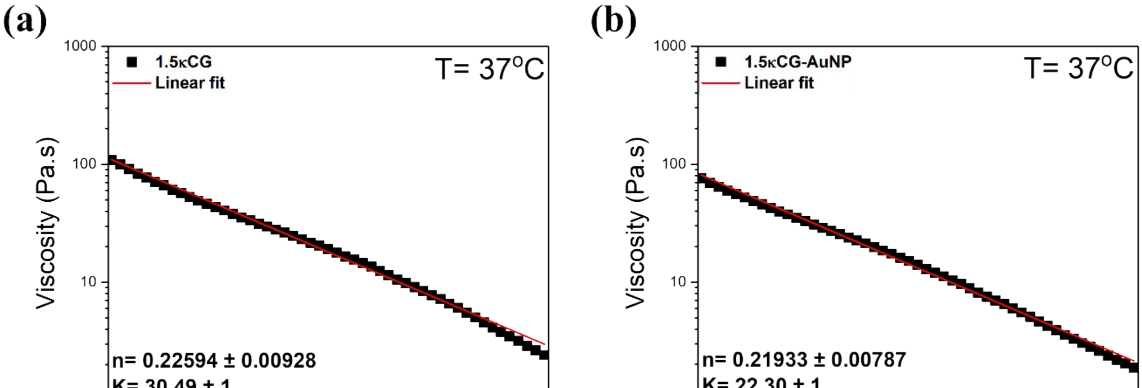

Fig S6. Linear model Power law fit of pre-extruded **(a)** pristine 1.5κCG and **(b)** 1.5κCG-AuNP hydrogels.

7. Determination of critical strain (γ_c) from large amplitude oscillatory strain sweeps

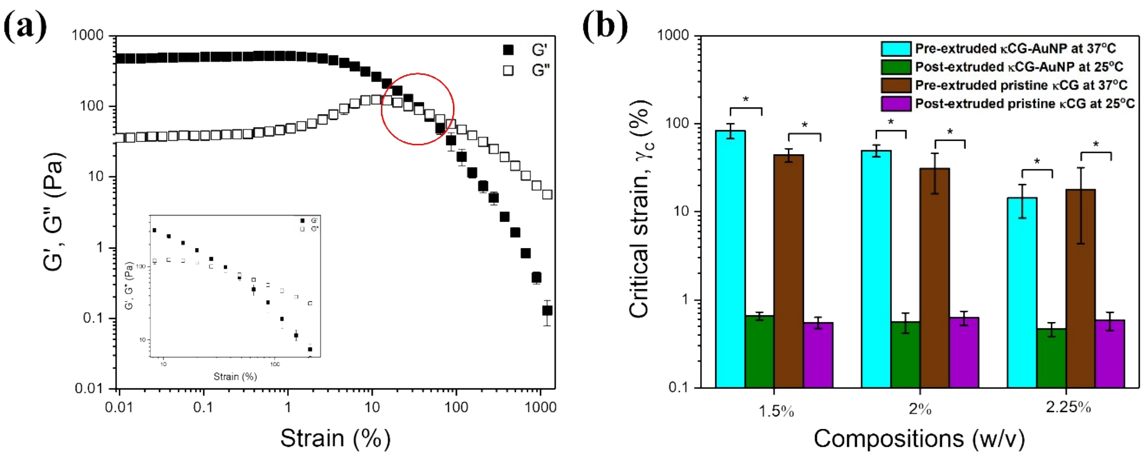

Fig S7. (a) Determination of critical strain (γ_c) from the crossover point of G′ and G″ of large amplitude oscillatory strain sweeps; **(b)** Comparison of γ_c of varying compositions of κCG-AuNP and pristine κCG hydrogels at 37 °C and after incubation in 100 mM KCl crosslinking bath at 25 °C.

8. Compressive modulus calculation

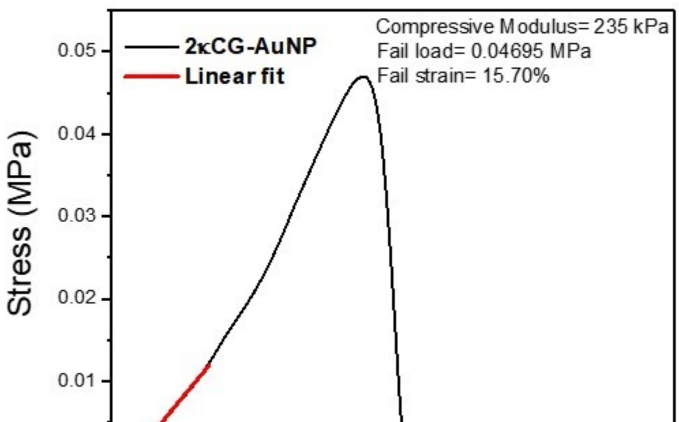

Fig S8. Linear fit of the stress-strain curve of 2κCG-AuNP hydrogel before crosslinking in 100 mM KCl bath.

9. Relaxation time measurement of κCG and κCG-AuNP hydrogels

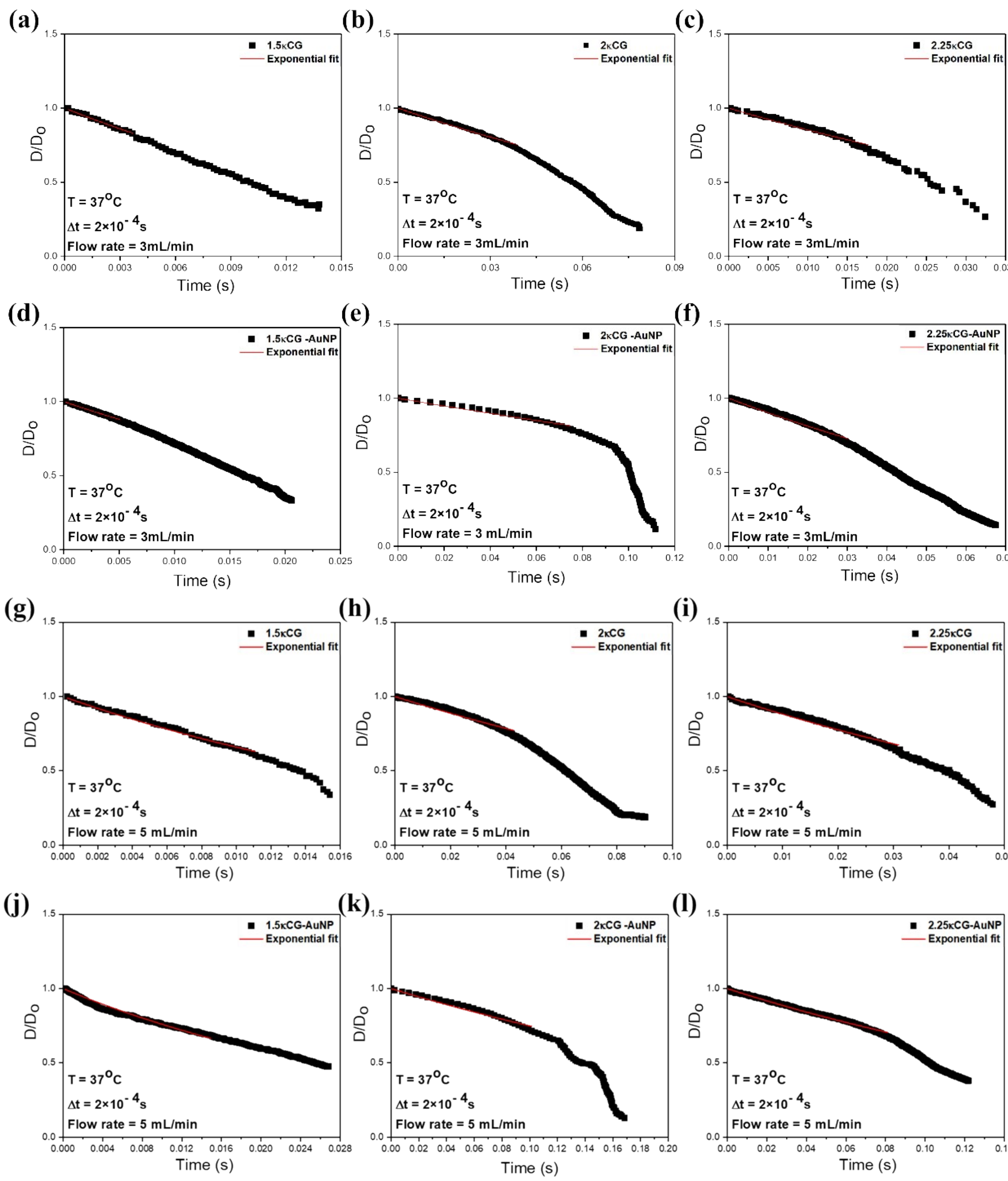

Fig S9. Exponential fit by Equation 4 of all compositions of κCG and κCG-AuNP at **(a-f)** 3 mL/min flow rate; **(g-l)** 5 mL/min flow rate.

10. Diameter decay profiles

(a)

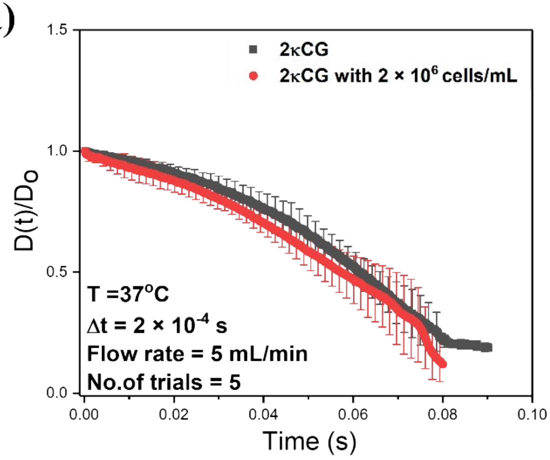

(b)

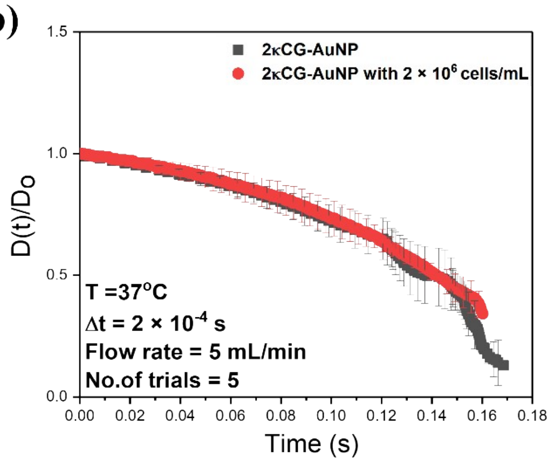

Fig S10. Diameter evolution over time plotted for A549 encapsulated and acellular **(a)** 2κCG hydrogel; **(b)** 2κCG-AuNP hydrogel.

Table S3. Relaxation time (λ) of 2 × 10^6 cells/mL of A549 encapsulated of pre-extruded 2κCG and 2κCG-AuNP hydrogels.

Composition	Relaxation time λ(s)	
	Acellular	Cellular
2κCG	0.055±0.003	0.042±0.001

2κCG-AuNP	0.1168±0.002	0.1165±0.001

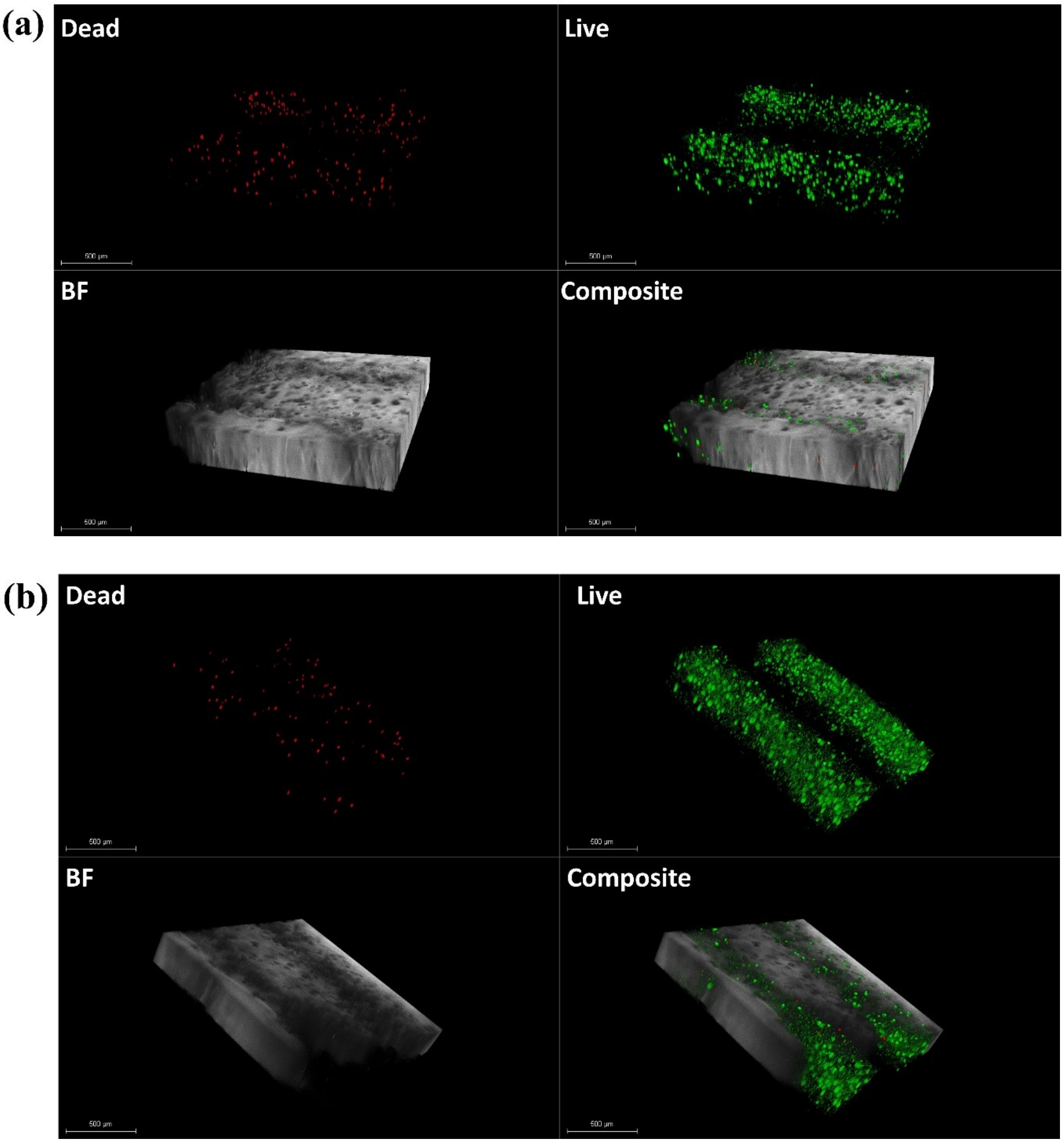

Fig S11. 3D z-stack images of cell-laden hollow conduits of **(a)** 2κCG hydrogel, **(b)** 2κCG-AuNP hydrogel.

Table S4. Depth wise quantification of cell distribution from confocal z-stack analysis of a representative 2κCG hollow conduit:

z-stack region (slice number)	Depth range (µm)	Live	Dead	Total	Cell Viability (%)
1-29 **(Top)**	0-67.48	179	80	259	69.11
30-58	67.48-134.96	151	69	220	68.64
59-87	134.96-202.44	156	92	248	62.90
88-116 **(Bottom)**	202.44-277.15	117	58	175	66.86

Table S5. Depth wise quantification of cell distribution from confocal z-stack analysis of a representative 2^{κ}CG-AuNP hollow conduit:

z-stack region (slice number)	**Depth range (µm)**	**Live**	**Dead**	**Total**	**Cell Viability (%)**
1-24 **(Top)**	0-55.43	175	56	231	75.76
25-48	55.43-110.86	167	47	214	78.04
49-72	110.86-166.29	154	38	192	80.21
73-95 **(Bottom)**	166.29-226.54	114	29	143	79.72

12. 2D control experiments for assessing KCl toxicity on A549 cells

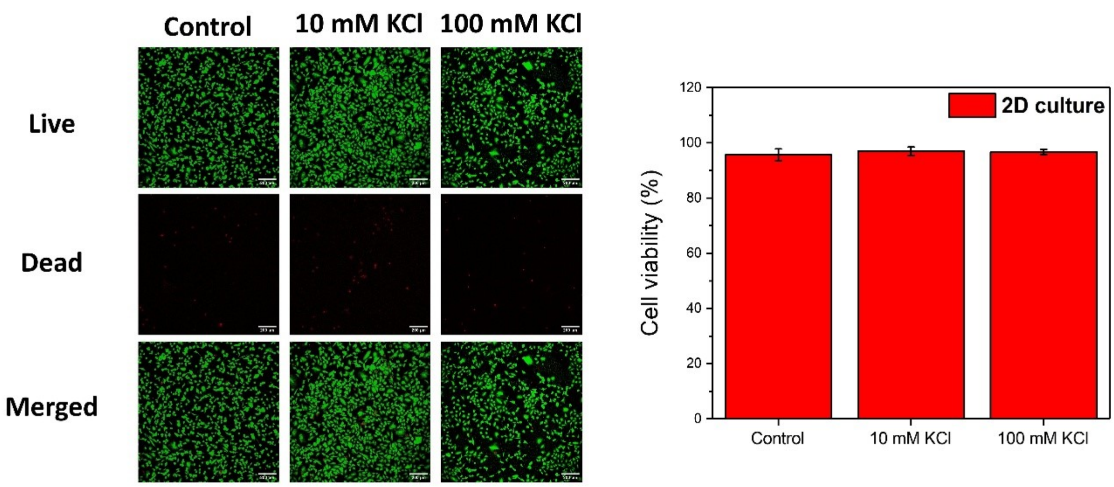

Fig S12. Maximum intensity z-stack images of A549 cells treated with 10 mM KCl for 24 hours and 100 mM KCl for half an hour at 4°C and their respective cell viabilities. Oneway analysis of variance with Tukey's test was used for comparison, and $p<0.05$ was considered statistically significant, indicated in the figure by '*' (n=3).